IEEE Access
Multidisciplinary | Rapid Review | Open Access Journal

Received January 26, 2021, accepted February 17, 2021, date of publication March 8, 2021, date of current version March 15, 2021.

Digital Object Identifier 10.1109/ACCESS.2021.3064315

High-Speed and Accurate Meat Composition Imaging by Mechanically-Flexible Electrical Impedance Tomography With *k*-Nearest Neighbor and Fuzzy *k*-Means Machine Learning Approaches

P. N. DARMA AND M. TAKEI, (Member, IEEE)
Division of Fundamental Engineering, Department of Mechanical Engineering, Graduate School of Science and Engineering, Chiba University, Chiba 263-8522, Japan

Corresponding author: M. Takei (masa2@chiba-u.jp)

ABSTRACT High-speed and accurate meat composition imaging method has been proposed based on mechanically-flexible electrical impedance tomography (*mech-f*-EIT) with k-nearest neighbor and fuzzy k-means machine learning approaches. This proposed method has four stages which are 1) estimation of meat boundary shape $\partial\Omega$ by *mech-f*-EIT for base data, 2) approximation of Jacobian matrix $\mathbf{J}^*$ by k-nearest neighbor (k-NN) algorithm under $\partial\Omega$ for high speed, 3) clustering of meat composition ${}^k\boldsymbol{\sigma}$ (fat $k = 1$, lean $k = 2$, bone $k = 3$) by fuzzy k-means algorithm based on the reconstructed meat conductivity distribution σ for high accuracy, and 4) edge detection of meat composition ${}^k\Omega$ by Canny algorithm for sharp edge. This method is qualitatively evaluated by using two agar phantoms, a cow's lower leg and three lamb's lower legs. As the results, *mech-f*-EIT estimates $\partial\Omega$ with total mean boundary error $\langle\widetilde{e_b}\rangle = 4.81$ %. This method achieves high-speed approximation of $\mathbf{J}^*$ with total mean speed-up performance $\langle\widetilde{sp}\rangle = 4.51$ times as compared with the computation time of standard $\mathbf{J}$; nonetheless, total mean cross correlation between $\mathbf{J}^*$ and $\mathbf{J}$ is accurate $\langle\widetilde{cc}\rangle = 0.92$. Moreover, this method clusters the ${}^k\boldsymbol{\sigma}$ with total mean area error $\langle\widetilde{e_a}\rangle = 4.49$ %. Furthermore, this imaging method detects sharply the meat composition edges ${}^k\Omega$ between fat and lean ($k = 1 - 2$) and between lean and bone ($k = 2 - 3$) with total mean edge error $\langle\widetilde{e_e}\rangle$ =6.90 %.

INDEX TERMS Electrical impedance tomography, k-nearest neighbor, fuzzy k-means, meat composition imaging.

I. INTRODUCTION

In meat industries, automatic meat cutting machine are already put into practice for alleviating the working environment [1]. The meat cutting machine require the high-speed and accurate clustering and edge detection of meat composition of fat, lean and bone to improve the cutting efficiency and quality. Usually, the cutting machine uses X-ray for the clustering and edge detection. More specifically, dual energy X-ray absorptiometry (DEXA) is used for clustering and edge detection of the meat composition [2], and the cross-sectional composition imaging [3]. On the other hand, magnetic resonance imaging (MRI) visualizes cross sectional images of living pig loin to predict body composition [4].

The associate editor coordinating the review of this manuscript and approving it for publication was Wuliang Yin.

In spite of the high spatial resolution of the conventional meat composition imaging methods, these methods have some drawbacks which are bulky, expensive, high power, and/or high radioactive [5].

In order to resolve the drawbacks, flexible electrical impedance tomography with flexible sensors (flexible EIT) has been applied for flexible boundary in human bodies such as patient's chest in lung imaging [6], patient's breast in breast cancer detection [7] and patient's stomach in gastroesophageal reflux detection [8]. The flexible EIT is handy, less expensive, low power consumption, and radiation free [9]. The flexible EIT has opened the possibility of real-time and portable meat composition imaging. However, the present flexible EIT does not satisfy with the minimum requirement of high-speed and accurate imaging in the clustering and edge detection because estimation of flexible boundary shape $\partial\Omega$

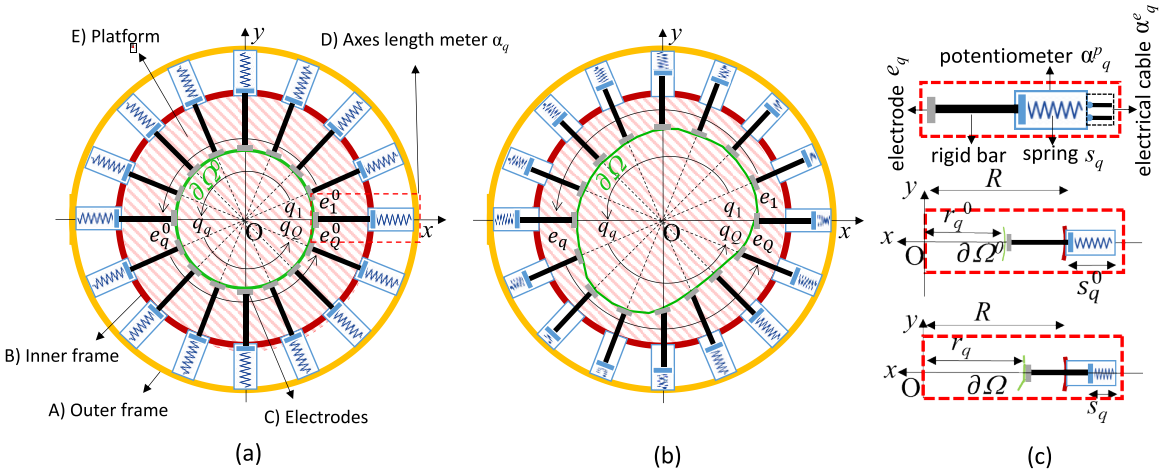

FIGURE 1. Structure of mechanically-flexible EIT (*mech-f*-EIT) sensor. (a) Default circular boundary shape $\partial\Omega^0$ (b) Meat boundary shape $\partial\Omega$ (c) Measurement principle of axes length meter α_q.

is not accurate and computation of Jacobian matrix $\mathbf{J}$ is slow. Generally, in order to improve the accuracy of $\partial\Omega$,external boundary sensors around $\partial\Omega$ are already proposed, which are the combination of stretch and angle detector sensors [10], bend-sensors [11], and inertial measurement unit (IMU) [12]. Another approach to improve the accuracy is numerical correction; for instance, finite element method (FEM) such as Fréchet derivative [13], naïve perturbation [14] and minimal perturbation [15] correct the error of $\partial\Omega$ based on the estimated $\partial\Omega$ by the numerical simulation. Moreover, in order to speed up the computation of $\mathbf{J}$, several hardware and software approaches are already proposed, which are a parallel graphical computing unit (GPU) [16], cluster computing and cloud computing [10].

However, these conventional improvement approaches for flexible EIT still have several negative points while they are applied to the meat composition imaging, which are 1) conventional flexible EIT sensor is not applicable for estimating meat boundary shape $\partial\Omega$ even though it is useful for estimating human boundary shape $\partial\Omega$ from the sanitary viewpoint, 2) estimation of $\partial\Omega$ and computation of $\mathbf{J}$ in flexible EIT are performed separately on a different platform which makes the process slow, and 3) the high-speed and accurate clustering ${}^k\boldsymbol{\sigma}$ and edge detection ${}^k\Omega$ of meat composition (fat $k = 1$, lean $k = 2$, bone $k = 3$) by using flexible EIT has not been established yet.

In order to solve the above-mentioned three negative points, this present research has proposed new approaches, which are mechanically-flexible electrical impedance tomography (*mech-f*-EIT) to solve the 1st point, implementation of k-nearest neighbor machine learning to solve the 2nd point, and implementation of fuzzy k-means machine learning to solve the 3rd point. Therefore, this present research has five objectives; which are firstly, 1) proposal of a high-speed and accurate meat composition imaging method called *mech-f*-EIT. Next, after applying the proposed *mech-f*-EIT to animal meats, qualitative evaluation is performed from four viewpoints; namely, 2) accuracy of estimated $\partial\Omega$, 3) computation speed of approximated $\mathbf{J}^*$, 4) accuracy of ${}^k\boldsymbol{\sigma}$, and 5) accuracy of ${}^k\Omega$.

II. HIGH-SPEED AND ACCURATE MEAT COMPOSITION IMAGING METHOD

A. STAGE I: ESTIMATION OF MEAT BOUNDARY SHAPE BY MECHANICALLY FLEXIBLE EIT

Figure 1 shows the structure of mechanically-flexible EIT (*mech-f*-EIT) which is composed of A) outer frame to attach electrical cables, B) inner frame with radius R to fix sensor position, C) Q number electrodes e_q for current injection and voltage measurement ($Q = 16$ as an example in the figure), D) Q number axes length meter α_q to measure the meat axes lengths r_q and E) platform to hold the meat firmly in position. **Figure 1(a)** shows a default circular boundary shape $\partial\Omega^0$. The axes length meters α_q are fixed between B) and A), then the rigid bar of α_q connects the electrode and potentiometer mechanically. Absolute origin O is the center of default circular boundary shape $\partial\Omega^0$. The x and y axes are defined as the absolute axes. The imaging area inside the *mech-f*-EIT is divided into Q quadrants $q_Q (Q = 16$ in the figure as an example from q_1 to $q_{16})$. The radius from O to $\partial\Omega^0$ in x-y coordinate are defined as $\mathbf{r}^0 = [r_1^0, \ldots, r_q^0 \ldots, r_Q^0] \in \mathbb{R}^Q$. **Figure 1(b)** shows an example of a $\partial\Omega$ after the meat is put on the E). The spring inside α_q presses the rigid bar so that the C) contacts the $\partial\Omega$. The O in x-y coordinate is fixed after $\partial\Omega^0$ is deformed to $\partial\Omega$. The axis lengths from O to $\partial\Omega$ in x-y coordinate are defined as $\mathbf{r} = [r_1, \ldots, r_q \ldots, r_Q] \in \mathbb{R}^Q$, which are measured by the α_q. **Figure 1(c)** shows the structure and measurement principle of α_q to measure electrodes moving length s_q from $\partial\Omega^0$ to $\partial\Omega$ which consists of 1) a potentiometer α_q^p to measure the electrical resistance of axes length from $\partial\Omega^0$ to $\partial\Omega$ on the platform, 2) a spring s_q to push the electrode toward $\partial\Omega$ automatically, 3) a rigid bar α_q^r to connect the electrode and potentiometer and 4) electrical cable α_q^e to send the resistance signal from the α_q to a personal computer (PC). Therefore, α_q measures the electrode moving length $\Delta r_q = r_q - r_q^0$ between r_q^0 and r_q in the deformation

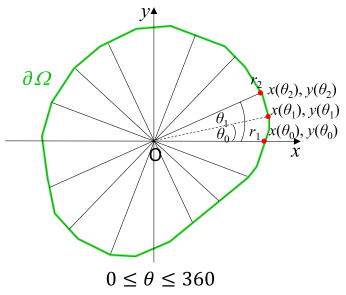

FIGURE 2. Flexible boundary shape ∂Ω estimation.

from $\partial\Omega^0$ to $\partial\Omega$. The Δr_q is calculated as

$$\Delta r_q = r_q^0 + (s_q^0 - s_q) \tag{1}$$

Figure 2 shows the (x, y) position of $\partial\Omega(x, y)$ estimated by

$$\partial\Omega(x_q, y_q) = \big(r_q \cos(\theta), r_q \sin(\theta)\big) \quad q = 1, 2, \ldots, Q \tag{2}$$

B. STAGE II: APPROXIMATION OF JACOBIAN MATRIX BY K-NN ALGORITHM

Figure 3 shows the flowchart to approximate Jacobian matrix $\mathbf{J}^*$ by k-nearest neighbor (k-NN) algorithm to achieve high-speed image reconstruction which consists of the pre-calculated dataset $\mathbf{I}$ and $\mathbf{J}$ as shown in **Figure 3(a)**, and approximation of $\mathbf{J}^*$ as shown in **Figure 3(b)**. The $\mathbf{I}$ under meat boundary shape $\partial\Omega^g$ at g-th geometry is defined as $\mathbf{I} = [\mathbf{I}^1, \ldots, \mathbf{I}^g, \ldots, \mathbf{I}^G] \in \mathbb{R}^{(Q+2)\times N\times G}$, where $\mathbf{I}^g = [\mathbf{I}^g_1, \ldots, \mathbf{I}^g_n, \ldots, \mathbf{I}^g_N] \in \mathbb{R}^{(Q+2)\times N}$, Q is the total number of electrodes, N is total number of mesh, and G is total number of geometry. The $\mathbf{I}^g_n$ is input variables on n-th mesh under g-th geometry, $\mathbf{I}^g_n = [\mathbf{X}^g_n, \mathbf{r}^g]^T \in \mathbb{R}^{(Q+2)}$ which consists the Cartesian coordinate of n-th mesh number under g-th geometry $\mathbf{X}^g_n = (x^g_n, y^g_n) \in \mathbb{R}^2$, and the radius of q-th electrode $\mathbf{r}^g = [r_1, \ldots, r_q, \ldots, r_Q] \in \mathbb{R}^Q$. The $\mathbf{J}$ under g-th geometry of meat boundary shape $\partial\Omega^g$ is defined as $\mathbf{J} = [\mathbf{J}^1, \ldots, \mathbf{J}^g, \ldots, \mathbf{J}^G] \in \mathbb{R}^{M\times N\times G}$ where $\mathbf{J}^g = [\mathbf{J}^g_1, \ldots, \mathbf{J}^g_n \ldots, J^g_N] \in \mathbb{R}^{M\times N}$ and $\mathbf{J}^g_n = [J^g_1, \ldots, J^g_m, \ldots, J^g_M]^T \in \mathbb{R}^M$ is a row vector of $\mathbf{J}$ under $\partial\Omega^g$.

The Jacobian matrix element J^g_{mn} at m-th measured voltage pattern at n-th mesh element is obtained by [17]

$$J^g_{mn} = \frac{\partial V^g_m}{\partial \sigma^g_n} = -\int_{\Omega^g} \nabla u(i^e) \bullet \nabla u(i^m) \mathrm{d}\Omega^g \tag{3}$$

where V^g_m is measured voltage at m-th measured voltage pattern ($1 \le m \le M$), σ^g_n is conductivity at n-th mesh ($1 \le n \le N$), $u(i^e)$ is the potential fields produced by injecting current i into the e-th electrode, $u(i^m)$ is the potential field produced by injecting current i from the m-th measured voltage pattern, and Ω^g is electrical field area inside the *mech-f*-EIT sensor.

The approximation of $\mathbf{J}^*$ under the estimated meat boundary shape $\partial\Omega$ by *mech-f*-EIT is defined as $\mathbf{J}^* = [\mathbf{J}^*_1, \ldots, \mathbf{J}^*_n, \ldots, \mathbf{J}^*_N] \in \mathbb{R}^{M\times N}$ where $\mathbf{J}^*_n = [J^*_1, \ldots, J^*_m, \ldots, J^*_M]^T \in \mathbb{R}^M$. The approximated Jacobian matrix element $J^*_{mn}(\mathbf{I}^*)$ as a function

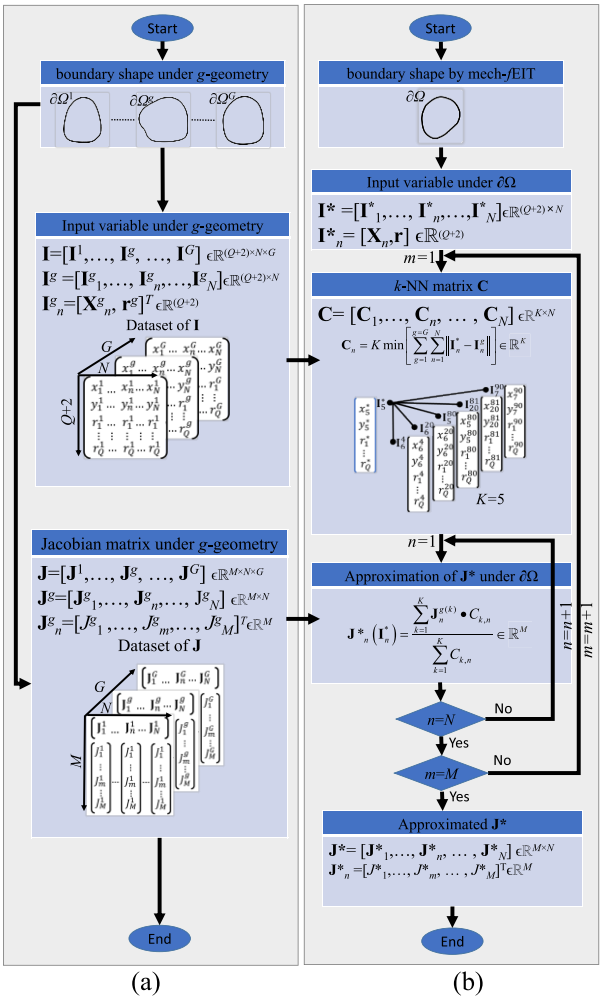

FIGURE 3. Flowchart to approximate Jacobian matrix J* by *k*-NN algorithm. (a) Pre-calculated dataset of I and J (b) Approximation of J*.

of $\mathbf{I}^* = [\mathbf{I}^*_1, \ldots, \mathbf{I}^*_n, \ldots, \mathbf{I}^*_N] \in \mathbb{R}^{(Q+2)\times N}$ under meat boundary shape $\partial\Omega$ at m-th measured voltage pattern and n-th mesh number by k-NN algorithm is expressed as

$$\mathbf{J}^*_n\left(\mathbf{I}^*_n\right) = \frac{\sum_{k=1}^{K} \mathbf{J}^{g(k)}_n \bullet C_{k,n}}{\sum_{k=1}^{K} C_{k,n}} \in \mathbb{R}^M \tag{4}$$

where $\mathbf{I}^*_n = [\mathbf{X}_n, \mathbf{r}]^T \in \mathbb{R}^{(Q+2)}$ is input variables on n-th mesh under $\partial\Omega$, which consists of the Cartesian coordinate of n-th mesh number and the radius of q-th electrode $\mathbf{r} = [r_1, \ldots, r_q, \ldots, r_Q] \in \mathbb{R}^Q$ measured by *mech-f*-EIT. The euclidean matrix $\mathbf{C} = [\mathbf{C}_1, \ldots, \mathbf{C}_n, \ldots, \mathbf{C}_N] \in \mathbb{R}^{K\times N}$ is defined as k set of $\mathbf{I}^g_n$ which has the shortest distance to $\mathbf{I}^*_n$ calculated using the following equation

$$\mathbf{C}_n = K \min \left[\sum_{g=1}^{g=G} \sum_{n=1}^{N} \left\| \mathbf{I}^*_n - \mathbf{I}^g_n \right\| \right] \in \mathbb{R}^K \tag{5}$$

K min operator in equation (5) means to pick up 1st to K-th minimum euclidean distance between $\mathbf{I}^g_n$ and $\mathbf{I}^*_n$.

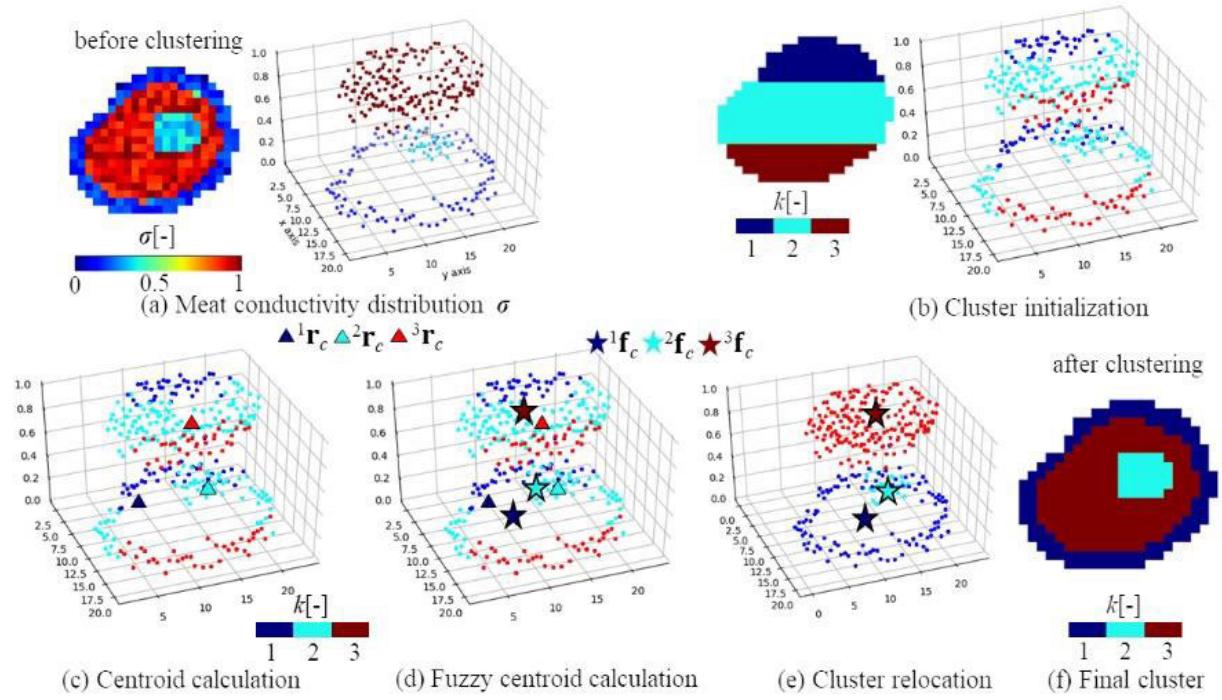

FIGURE 4. Clustering of meat composition ${}^{k}\sigma$ by fuzzy k-means algorithm.

C. STAGE III: CLUSTERING OF MEAT COMPOSITION BY FUZZY K-MEANS ALGORITHM

Figure 4 shows the process of clustering meat composition ${}^{k}\sigma$ (fat $k = 1$, lean $k = 2$, bone $k = 3$) by fuzzy k-means algorithm. **Figure 4(a)** shows the meat conductivity distribution $\sigma \epsilon \mathbb{R}^{Nx \times Ny}$ rearranged from $\sigma \epsilon \mathbb{R}^{N}$ where $N = 20 \times 25$ pixels as an example in the above **Figure 4**. **Figure 4(b)** shows the cluster initialization process as the 1st step which clusters σ into three clusters of initial fat cluster ${}^{1}\sigma^{0}$, initial lean meat cluster ${}^{2}\boldsymbol{\sigma}^{0}$, and initial bone cluster ${}^{3}\boldsymbol{\sigma}^{0}$. **Figure 4(d)** shows the fuzzy centroid calculation process as the 2nd step which calculates fuzzy centroid position of k-th cluster ${}^{k}\mathbf{f}_c$ from the n-th mesh element position vector ${}^{k}\mathbf{r}_n = (x_n, y_n)$ is expressed as

$$ {}^{k}\mathbf{f}_c^{j} = \sum_{n=1}^{n=nk} \left({}^{k}\mu_n^{j}\right)^2 {}^{k}\sigma_n \mathbf{r}_n \Big/ \sum_{n=1}^{n=nk} \left({}^{k}\mu_n^{j}\right)^2 \tag{6} $$

where ${}^{k}\sigma_n$ is k-th segmented conductivity distribution elements, ${}^{k}\mu_n^{j}$ is the fuzzy weighting of ${}^{k}\sigma_n$ calculated using the following equations

$$ {}^{k}\mu_n^{j} = 1 \Big/ \sum_{l=1}^{l=k} \left(\frac{\left\| \mathbf{r}_n - {}^{k}\mathbf{r}_{\mathbf{c}}^{j} \right\|}{\left\| \mathbf{r}_n - {}^{l}\mathbf{r}_{\mathbf{c}}^{j} \right\|} \right)^2 \tag{7} $$

$$ {}^{k}\mathbf{r}_c^{j} = \sum_{n=1}^{n=nk} {}^{k}\sigma_n \mathbf{r}_n \Big/ \sum_{n=1}^{n=nk} {}^{k}\sigma_n \tag{8} $$

where ${}^{k}\mathbf{r}_{\mathbf{c}}^{j}$ is k-th clustered centroid position calculated using equation (7) as shown in **Figure 4(c)**, j is fuzzy k-means iteration number and nk is total element of ${}^{k}\boldsymbol{\sigma}$.

Figure 4(e) shows the cluster relocation process as the 3rd step which relocates the conductivity distributions of clustered meat composition ${}^{k}\boldsymbol{\sigma}_n$ after a new fuzzy centroid position ${}^{k}\mathbf{f}_c$ is obtained. In this process, the elements of ${}^{k}\boldsymbol{\sigma}_n$ are relocated into a new clustered conductivity distribution by calculating Euclidean (L2) distance between the position of $\mathbf{r}_n$ and ${}^{k}\mathbf{f}_c$ by

$$ {}^{k}\boldsymbol{\sigma} = \arg\min \sum_{k=1}^{k=K} \sum_{n=1}^{N} ({}^{k}\mu_n^{j})^2 \left\| \mathbf{r}_n - {}^{k}\mathbf{f}_c^{j} \right\|^2 \tag{9} $$

The final clustered conductivity distribution is achieved when there is no difference in the L2 between ${}^{k}\mathbf{r}_n^{j}$ and ${}^{k}\mathbf{r}_n^{j+1}$ by using the following equation

$$ {}^{k}\mathbf{f}_c^{j+1} - {}^{k}\mathbf{f}_c^{j} = 0 \tag{10} $$

Figure 4(f) shows the final clustered conductivity distribution ${}^{k}\boldsymbol{\sigma}$. The meat composition area percentage ${}^{k}\eta$ [%] is defined based on k-th clustered conductivity distribution ${}^{k}\boldsymbol{\sigma}$ as

$$ {}^{k}\eta = \frac{{}^{k}A}{A} \times 100[\%] \tag{11} $$

where ${}^{k}A$ is area of k-th meat composition based on the clustered conductivity distribution and A is the total area of the meat.

D. STAGE IV: EDGE DETECTION OF MEAT COMPOSITION BY CANNY ALGORITHM

Figure5 shows the edge detection of meat composition by Canny algorithm [18]. Canny algorithm is dependent on conductivity gradient $\nabla\sigma_n$ calculated at every n-th pixel of

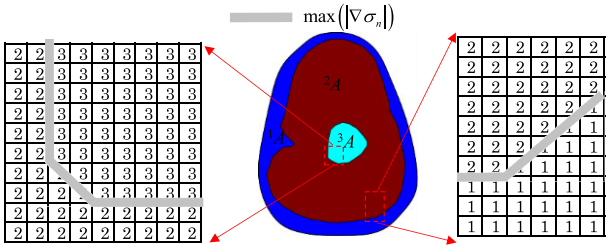

FIGURE 5. Edge detection by Canny algorithm.

segmented conductivity distribution ${}^k\sigma_n$ obtained by fuzzy k-means segmentation algorithm in the stage III. Initially, Sobel gradient matrix operator [19] is used for $\nabla\sigma_n$ calculation which contains two directional filters as

$$\mathbf{S}_x = \begin{bmatrix} -1 & 0 & 1 \\ -2 & 0 & 2 \\ -1 & 0 & 1 \end{bmatrix}, \quad \mathbf{S}_y = \begin{bmatrix} -1 & -2 & -1 \\ 0 & 0 & 0 \\ 1 & 2 & 1 \end{bmatrix} \tag{12}$$

where $\mathbf{S}_x$ and $\mathbf{S}_y$ are the Sobel gradient matrix operator along horizontal and vertical direction respectively. Combining these bidirectional filter, the conductivity gradient magnitude $|\nabla\sigma_n|$ is expressed by

$$|\nabla\sigma_n| = \sqrt{\left[(\boldsymbol{\sigma} * \mathbf{S}_x)_n\right]^2 + \left[\left(\boldsymbol{\sigma} * \mathbf{S}_y\right)_n\right]^2} \tag{13}$$

where, $\boldsymbol{\sigma} \in \mathbb{R}^{Nx \times Ny}$ is rearranged from ${}^k\boldsymbol{\sigma} \in \mathbb{R}^N$ obtained from equation (9), which is the two-dimensional segmented conductivity distribution image with pixel number $Nx \times Ny = N$, the operation $(\,)_n$ means to pick up the value of n-th $\boldsymbol{\sigma}$, and $*$ symbol is the convolution operator. The maximum $|\nabla\sigma_n|$ which is the largest conductivity change shows the edge Ω_n on n-th pixel as

$$\Omega_n = \begin{cases} 1, & \text{in the case of } |\nabla\sigma_n| = \max\left(|\nabla\sigma_n|\right) \\ 0, & \text{in the case of } |\nabla\sigma_n| \neq \max\left(|\nabla\sigma_n|\right) \end{cases} \tag{14}$$

III. EXPERIMENTAL SETUP, METHOD AND CONDITION

A. EXPERIMENTAL SETUP

Figure 6 shows the EIT experimental setup consisting of a) an impedance analyzer (IM 3570 manufactured by Hioki E.E Corporation Japan), b) an electrical tomography multiplexer developed in Takei Laboratory by using an Arduino Due microcontroller and CD74HC4067 (Texas Instrument USA) Analog Mux/Demux, c) *mech-f*-EIT sensor, and d) personal computer (PC).

The a) impedance analyzer was connected to an electrical tomography multiplexer by using four ports: Hc, Hp, Lc, and Lp. The b) electrical tomography multiplexer was connected to the 16 electrodes of the *mech-f*-EIT sensor by using coaxial cable. The coaxial cable was twisted with the adjacent cable to eliminate the induction cable at high frequency. The voltage measurements $\mathbf{V}$ from impedance analyzer and axes length $\mathbf{r}$ from *mech-f*-EIT were sent to PC by using a USB cable.

The c) *mech-f*-EIT sensor was composed of an inner frame with diameter $d = 120$ mm, the outer frame of diameter

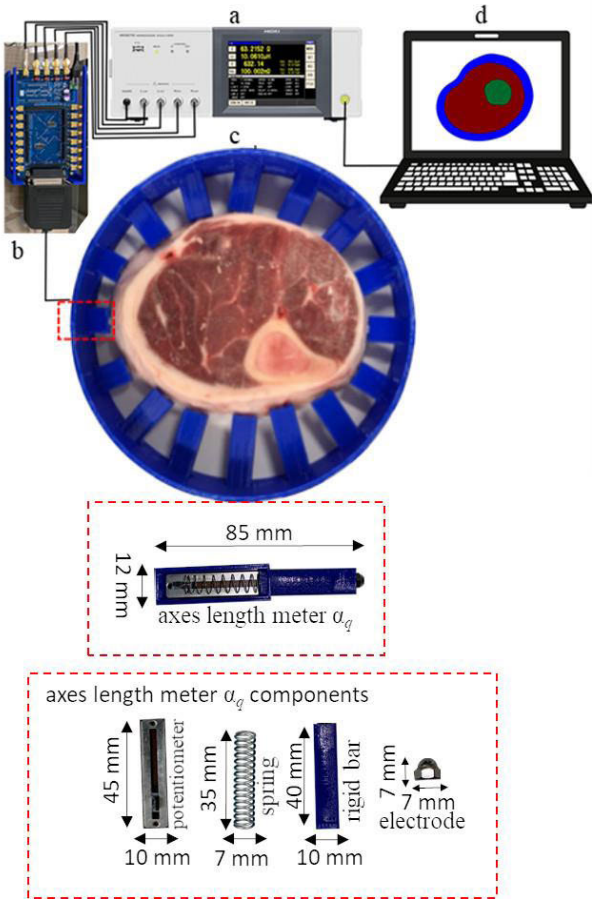

FIGURE 6. Experimental setup.

$d = 160$ mm, $E = 16$ number of round shape electrodes with $d = 7$ mm attached at the end of the rigid bar, therefore the total measured voltage pattern $M = 208$ were obtained from $M = Q(Q-3)$. $Q = 16$ number of axes length meter α_q were attached between inner frame and outer frame to measure the axes length r_q which consist of 10 kΩ potentiometer with length $l_x = 45$ mm and wide $l_y = 10$mm, spring s_q with length $l_x = 35$ mm and wide $l_y = 7$ mm, rigid bar with length $l_x = 45$ mm and wide $l_y = 10$ mm.

The d) Personal computer (Microsoft Surface 2 laptop) with 1.7GHz Intel Core i5-8250U (quad-core, 6MB cache, up to 3.4GHz boost) and 8 Gb RAM was used in the estimation of flexible boundary shape $\partial\Omega$, approximation of Jacobian matrix $\mathbf{J}^*$, clustering of meat composition ${}^k\boldsymbol{\sigma}$ and edge detection of meat composition ${}^k\Omega$.

B. EIT EXPERIMENTAL CONDITION AND METHOD

Figure 7 shows two agar phantoms, one sliced lower leg of a cow, and three sliced lamb's lower legs. The agar phantoms were composed of a mimic fat, a lean meat, and a bone whose conductivities were adjusted to $\sigma_{\text{fat}} = 0.024$ S/m, $\sigma_{\text{lean}} = 0.351$ S/m, and $\sigma_{\text{bone}} = 0.083$ S/m, respectively [20]. Each conductivity was adjusted by mixing distilled

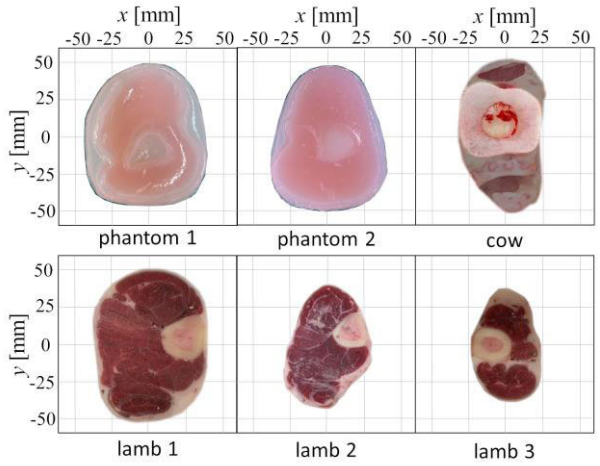

FIGURE 7. Agar phantoms, cow and lamb meats.

water, NaCl and agar powder (Laboratory Grade, A360 Fisher Scientific) under agar melting temperature 85 °C [21]. The frozen cow and lamb upper leg meats delivered from New Zealand (Newzee Company www.newzee.com) were naturally thawed under room temperature before the experiments.

The $(i+1)$-th iterative meat conductivity distribution $\sigma^{i+1} \epsilon \mathbb{R}^N$ was calculated with the approximated Jacobian matrix $\mathbf{J}^*$ by

$$\boldsymbol{\sigma}^{i+1} = \boldsymbol{\sigma}^{i} - (\mathbf{J}^{*\mathrm{T}}\mathbf{J}^{*} + \lambda\mathbf{R})^{-1}\mathbf{J}^{*\mathrm{T}}\Delta\mathbf{V} \tag{15}$$

$\mathbf{R}$ is a regularization matrix, and λ is a relaxation factor scalar which automatically determined using L-Curve method [22], $\Delta\mathbf{V} = [\Delta V_1, \ldots, \Delta V_m, \ldots, \Delta V_M]^T \epsilon \mathbb{R}^M$ is the normalized measured voltage between the voltage in lower frequency $\mathbf{V}(f_0)$ and voltage in higher frequency $\mathbf{V}(f_1)$ under meat boundary shape $\partial\Omega$ which is written by

$$\Delta V_m(f_1 - f_0) = \frac{V_m(f_1) - V_m(f_0)}{V_m(f_0)} \tag{16}$$

where m is measured voltage pattern. The initial conductivity image $\boldsymbol{\sigma}^0$ is obtained from linear back projection (LBP) algorithm written by

$$\boldsymbol{\sigma}^0 = \mathbf{J}^{*T}\Delta\mathbf{V} \tag{17}$$

The running time $t(\mathbf{J})$ is defined as the time required to compute Jacobian matrix $\mathbf{J}$ in equation (3) by using FreeFEM simulation software [23] and t($\mathbf{J}^*$) is defined as running time to approximate Jacobian matrix by using k-NN algorithm. The t starts ($t = 0$) from the estimation of meat boundary shape $\partial\Omega$ (stage I) and finishes when Jacobian matrix $\mathbf{J}^*$ is approximated ($t = t$) (stage III). The t is an indicator for the performance between standard Jacobian matrix $\mathbf{J}$ and approximated Jacobian matrix $\mathbf{J}^*$. Pre-calculated datasets of $\mathbf{I}$ and $\mathbf{J}$ are obtained by finite element method (FEM) simulation with $G = 200$ number of random geometry, which stored totally 150 Gigabyte.

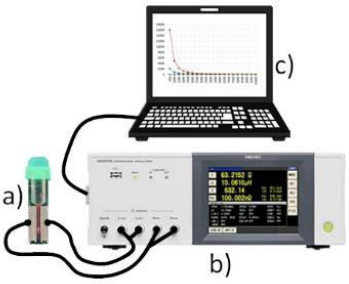

FIGURE 8. EIS experiment setup.

C. EIS EXPERIMENTAL CONDITION AND METHOD

In frequency different EIT using two different frequency pairs as shown in equation (16), the essential factor influencing image reconstruction is frequency-dependent of conductivity distributions object to be imaged. Therefore, Electrical Impedance Spectroscopy (EIS) method [24], [25] is used to optimize frequency pairs determination (f_0 and f_1) based on the frequency-dependent of meat ${}^k\sigma(f)$ conductivity (fat $k = 1$, lean $k = 2$, bone $k = 3$). **Figure 8** shows EIS experiment setup consisting of the a) NEPA electroporation cuvette (NEPA EE, Japan) were used to hold the lean, fat, and bone samples, the b) Impedance Analyzer (IM 3570 manufactured by Hioki E.E Japan) is used to measure the complex impedance between 500 Hz and 10 KHz range with 2 mA constant current setting, and the c) personal computer (PC).

In order to quantitatively evaluate the frequency-dependent of meat conductivity by EIS, conductivity change ratio $\Delta^k\sigma(f_1 - f_0)$ is defined using the following equation:

$$\Delta^k\sigma(f_1 - f_0) = \left| \frac{{}^k\sigma(f_1) - {}^k\sigma(f_0)}{{}^k\sigma(f_0)} \right| \times 100\% \tag{18}$$

where ${}^k\sigma(f)$ is the frequency-dependent of meat conductivity (fat $k = 1$, lean $k = 2$, bone $k = 3$), ${}^k\sigma(f_0)$ is the conductivity of meat in lower frequency, and ${}^k\sigma(f_1)$ is the conductivity of meat in higher frequency.

IV. EXPERIMENTAL RESULTS AND DISCUSSION

A. ESTIMATION OF MEAT BOUNDARY SHAPE

As the experimental result of Stage I: estimation of meat boundary shape by *mech-f*-EIT, **Figure 9** shows the comparison between the true meat boundary shape $\partial\Omega^{\mathrm{true}}$ (black dotted line) and the estimated meat boundary shape $\partial\Omega$ by *mech-f*-EIT (solid blue line). As shown in this figure, the $\partial\Omega$ is qualitatively close to the $\partial\Omega^{\mathrm{true}}$. In order to evaluate the accuracy of $\partial\Omega$, the boundary error e_b [%] is defined as

$$e_b = \frac{\partial\Omega - \partial\Omega^{\mathrm{true}}}{\partial\Omega^{\mathrm{true}}} \times 100\,[\%] \tag{19}$$

The ideal condition is $e_b = 0.0\%$, which means that the $\partial\Omega$ and the $\partial\Omega^{\mathrm{true}}$ are identical. The bar chart in **Figure 9** shows the comparison of e_b for agar phantoms, cow and lamb meats. The $e_b = 3.46\%$, 3.38%, 10.57%, 3.02%, 3.19% and 5.35% respectively for phantom 1, phantom 2, cow, lamb 1, lamb 2 and lamb 3. The total mean error boundary $\langle \tilde{e}_b \rangle$ is 4.81%,

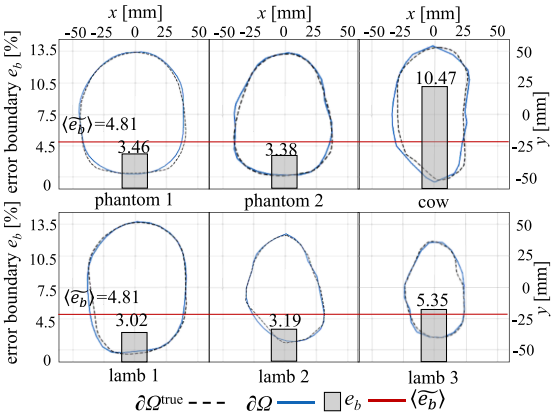

FIGURE 9. Estimation of meat boundary shape $\partial\Omega$ by *mech-f*-EIT.

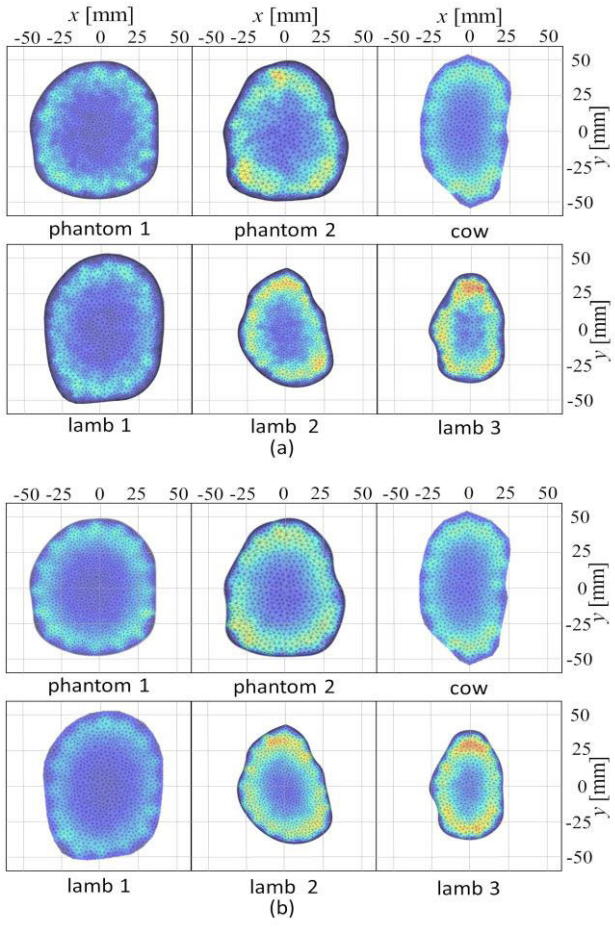

FIGURE 10. Axial plot of Jacobian matrix (a) Axial plot of true Jacobian matrix J (b) Axial plot of approximated Jacobian matrix J*.

which is relatively small. As a result, *mech-f*-EIT estimates $\partial\Omega$ close to $\partial\Omega^{\text{true}}$.

B. APPROXIMATION OF JACOBIAN MATRIX BY K-NN ALGORITHM

As the experimental result of Stage II: approximation of Jacobian matrix $\mathbf{J}^*$ by k-NN algorithm, **Figure 10** shows the comparison between the axial plot of true Jacobian matrix $\mathbf{J}$

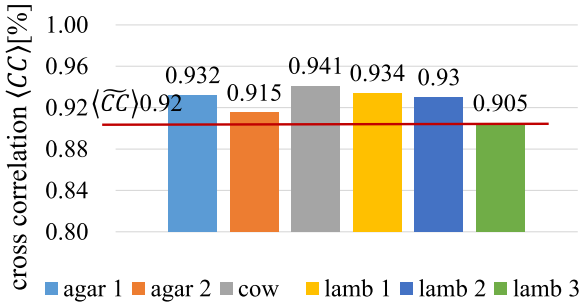

FIGURE 11. Comparison of cross correlation $\langle CC \rangle$.

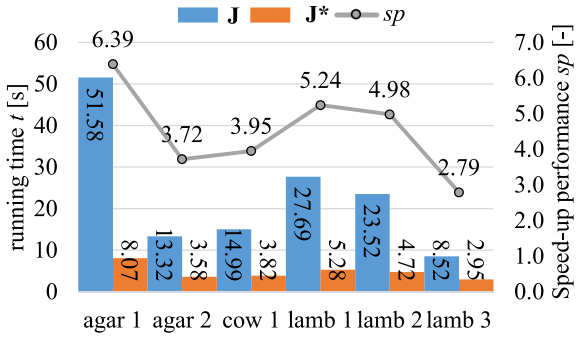

FIGURE 12. Comparison of running time t and speed-up performance sp.

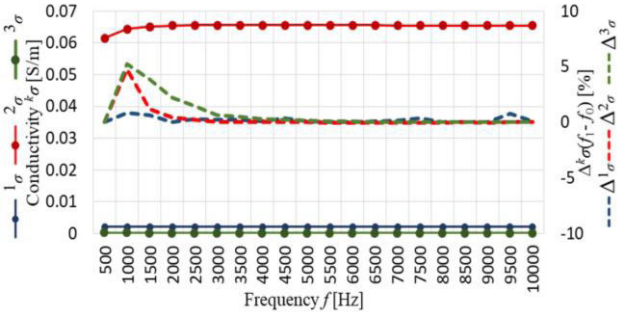

FIGURE 13. EIS experiment results.

and approximated Jacobian matrix $\mathbf{J}^*$ for agar phantoms, cow and lamb meats.

In order to estimate the similarity between $\mathbf{J}^*$ and $\mathbf{J}$, the mean cross correlation $\langle CC \rangle$ is expressed by

$$\langle CC \rangle = \frac{1}{M} \sum_{m=1}^{m=M} \frac{\left[(\mathbf{J}_m - \langle \mathbf{J}_m \rangle)(\mathbf{J}_m^* - \langle \mathbf{J}_m^* \rangle) \right]}{\sqrt{\left[(\mathbf{J}_m - \langle \mathbf{J}_m \rangle)^2 - (\mathbf{J}_m^* - \langle \mathbf{J}_m^* \rangle)^2 \right]}} [-] \tag{20}$$

where, $<\mathbf{J}>$ and $<\mathbf{J}^*>$ are average of Jacobian matrix and average of approximated Jacobian matrix respectively, the total measured voltage pattern $M = 208$. The ideal condition is $\langle CC \rangle = 1.0$ which means $\mathbf{J}^*$ and $\mathbf{J}$ are identical. The bar chart in **Figure 11** shows $\langle CC \rangle$ values of agar phantoms, cow and lamb meats calculated from equation (19).

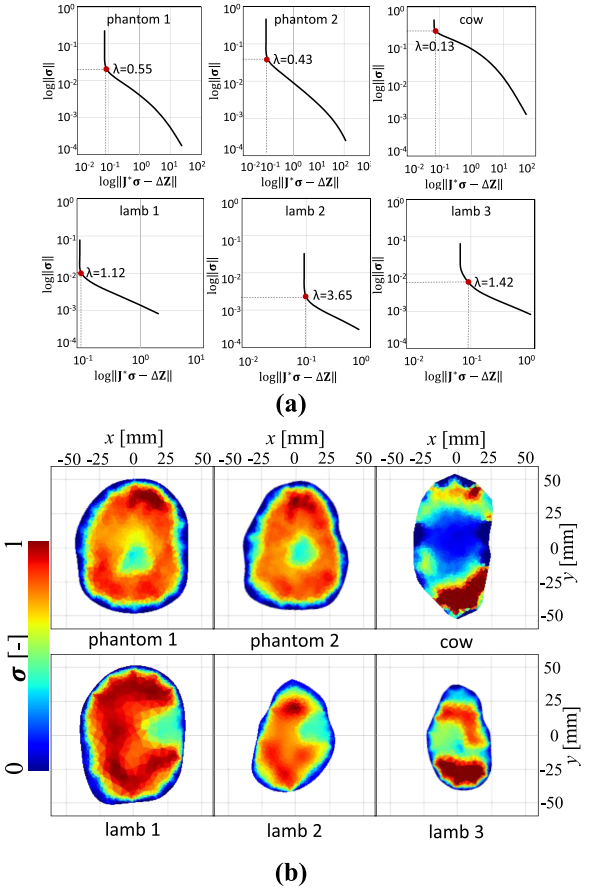

FIGURE 14. (a) L-curve to estimate optimum λ. (b) Reconstructed meat conductivity distribution.

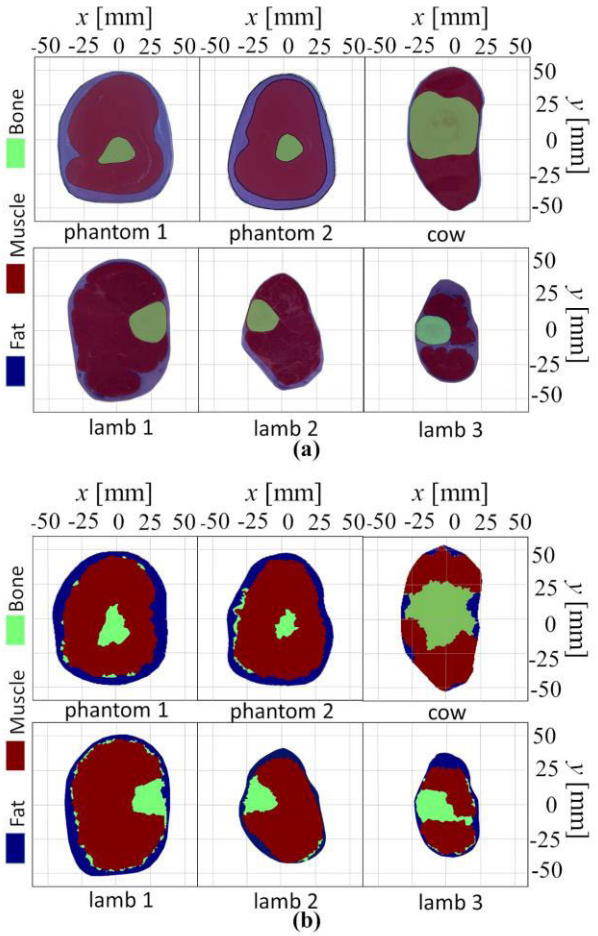

FIGURE 15. Clustered meat composition. (a) True meat composition ${}^{k}\sigma^{\text{true}}$ (b) Clustered conductivity distribution ${}^{k}\sigma$ by fuzzy k-means.

The $\langle CC \rangle$ achieves to $\langle CC \rangle = 0.93, 0.91, 0.93, 0.93$ and 0.90 for phantom 1, phantom 2, cow, lamb 1, lamb 2 and lamb 3 respectively with total mean of cross correlation $\langle \widetilde{CC} \rangle = 0.92$, which means that $\mathbf{J}^*$ has high similarity with $\mathbf{J}$.

The bar chart in **Figure 12** shows the running time t of $\mathbf{J}^*$ (orange bar) and $\mathbf{J}$(blue bar). From this figure, the running time of $\mathbf{J}^*$ is faster than $\mathbf{J}$ from $t = 51.58$s to $t = 8.07$s, from $t = 13.32$s to $t = 3.58$s, from $t = 14.99$s to $t = 3.82$s, from $t = 27.69$s to $t = 5.28$s, from $t = 23.52$s to $t = 4.72$s, from $t = 8.25$s to $t = 2.95$s respectively for phantom 1, phantom 2, cow, lamb 1, lamb 2 and lamb 3.

In order to evaluate the computation efficiency of $\mathbf{J}^*$, speed-up performance sp[-] is defined as

$$sp = \frac{t(\mathbf{J})}{t(\mathbf{J}^*)}[-] \tag{21}$$

where $t(\mathbf{J}^*)$[s] is running time of $\mathbf{J}^*$ computations and $t(\mathbf{J})$[s] is running time of $\mathbf{J}$ computation. The grey dot line in **Figure 12** shows the sp. The sp achieves up to $sp = 6.39$, 3.72, 3.93, 5.24, 4.98 and 2.79[-] for phantoms 1 and 2, cow, lamb legs 1, 2 and 3 respectively with the total mean of speed-up performance $\langle \widetilde{sp} \rangle = 4.51$. As a result, k-NN algorithm achieves high-speed approximation of $\mathbf{J}^*$; nonetheless, total mean cross correlation $\langle \widetilde{CC} \rangle$between $\mathbf{J}^*$ and $\mathbf{J}$ is high.

C. CLUSTERING OF MEAT COMPOSITION BY FUZZY K-MEANS ALGORITHM

The solid dotted line in the **Figure 13** shows measured conductivity ${}^{k}\sigma$ frequency-dependent responses of fat (solid blue dotted line), lean (solid red dotted line), and bone (solid green dotted line) as explained in the EIS experiment section (Section III.C), while the dashed line shows the conductivity change ratio $\Delta^{k}\sigma(f_1 - f_0)$ between higher and lower frequency of fat (blue dashed line), lean (red dashed line), and bone (green dashed line).The **Figure 13** indicates that the conductivity change ratio $\Delta^{k}\sigma(f_1 - f_0)$ becomes the maximum between $f_0 = 500$Hz and $f_1 = 1$Khz with 0.88 %, 4.79 %, and 5.23% conductivity change of fat, lean and bone, respectively. Hence, $f_0 = 500$Hz and $f_1 = 1$Khz were chosen for lower and higher frequency pair of frequency different EIT in **equation (16)**.

Based on the experimental results of Stage III: clustering of meat composition by fuzzy k-means algorithm, **Figure 14(a)** shows the L-curve used to estimate the optimal relaxation factor λ in the reconstructed conductivity distribution images σ by equation (15). **Figure 14(b)** shows the reconstructed conductivity distribution images σ based on the $\mathbf{J}^*$, compared

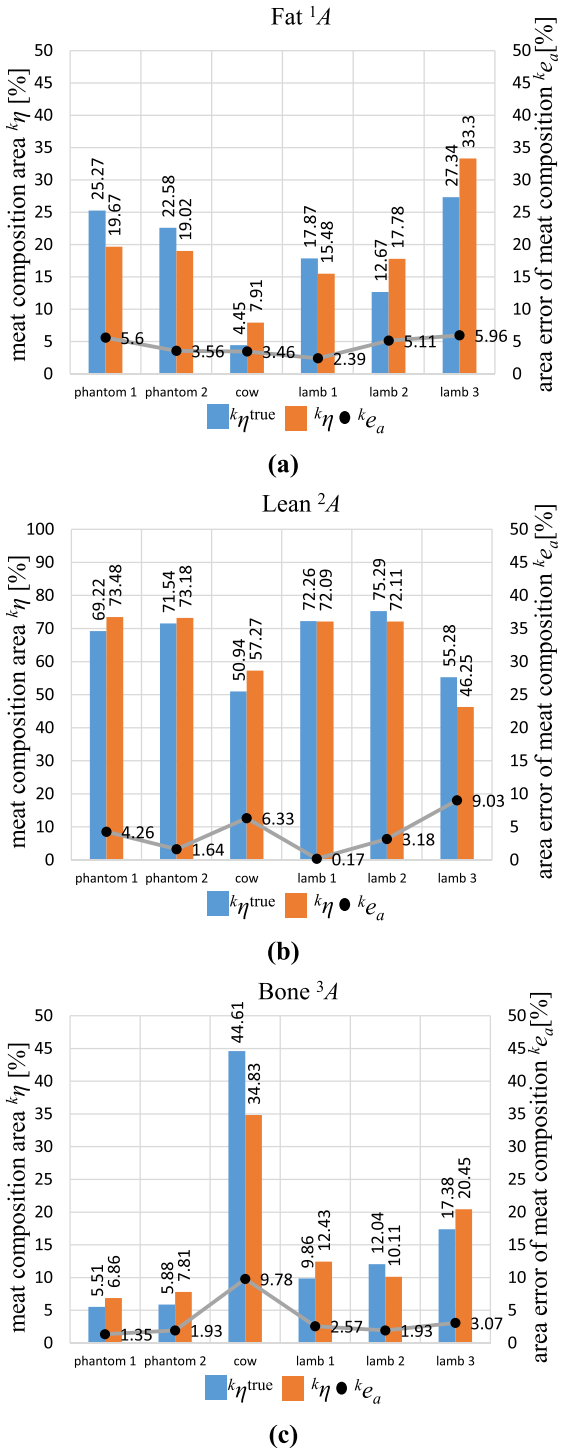

FIGURE 16. Clustered meat composition percentage $^k\eta$, true meat composition percentage $^k\eta^{\text{true}}$, and area error of meat composition ^ke_a.

with the true images σ^{true} of agar phantoms, cow and lamb meat as shown in **Figure 7**, the three meat compositions which are fat, lean meat and bone are qualitatively imaged.

Figure 15(a) shows the true meat composition $^k\sigma^{\text{true}}$ obtained by colouring pixels of the original meat photograph with its respective composition (blue=fat, red=lean, green=bone) employing image overlaying technique [26]. **Figure 15(b)** shows the clustered conductivity distribution images $^k\boldsymbol{\sigma}$ by fuzzy k-means algorithm based on the reconstructed conductivity distribution images σ shown in **Figure 14(b)**. It can be seen that the $^k\boldsymbol{\sigma}$ are qualitatively close to $^k\boldsymbol{\sigma}^{\text{true}}$.

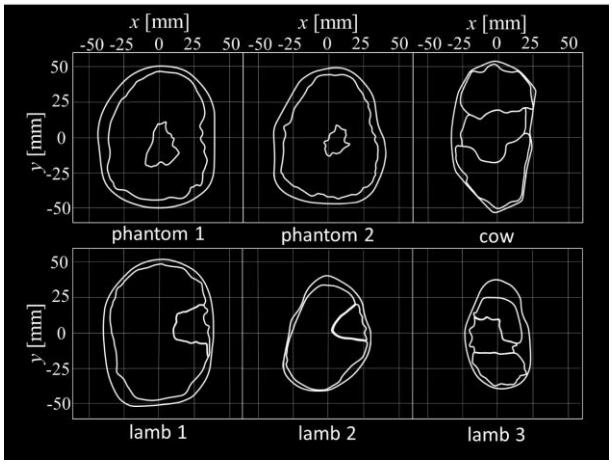

FIGURE 17. Meat composition edges $^k\Omega$ by Canny algorithm.

In order to evaluate the clustered meat composition, meat composition percentage $^k\eta$ is calculated using equation (11). The bar chart in **Figures 16(a), 16(b)** and **16(c)** show $^k\eta$ (orange bar chart) and the true meat composition percentage $^k\eta^{\text{true}}$ (blue bar chart) for fat, lean meat and bone. The $^k\eta^{\text{true}}$ was obtained from the true meat composition $^k\boldsymbol{\sigma}^{\text{true}}$ shown in **Figure 15(a)**. From **Figure 16**, it can be seen that the $^k\eta$ quantitatively close to $^k\eta^{\text{true}}$.

In order to evaluate the accuracy of $^k\boldsymbol{\sigma}$, area error ^ke_a is defined as

$$^ke_a = \left| ^k\eta - \frac{^kA^{\text{true}}}{A^{\text{true}}} \right| \times 100[\%] \tag{22}$$

where $^kA^{\text{true}}$ is the k-th area of true meat composition, A^{true} is the total area of phantoms and meat samples. The black dot mark in **Figure 16** shows ^ke_a calculated from equation (22). The mean area error are $^1e_a = 5.95\%$, $^2e_a = 4.10\%$ and $^3e_a = 3.44\%$ respectively for fat, lean meat and bone. The total mean area error $<^k\widetilde{e}_a>$ is achieved at only 4.49 %. As a result, fuzzy k-means algorithm achieves an accurate clustered $^k\boldsymbol{\sigma}$ close to $^k\boldsymbol{\sigma}^{\text{true}}$.

D. DETECTION OF MEAT COMPOSITION EDGE BY CANNY ALGORITHM

As the experimental result of Stage IV: detection of the edge of the meat composition by Canny algorithm, **Figure 17** shows the meat composition edge $^k\Omega$ calculated from equations (12) to (14) based on the clustered conductivity distribution $^k\boldsymbol{\sigma}$ shown in **Figure 15 (b)**. As depicted in the figure, the lean meat, fat and bone edge from agar phantoms, cow and lamb meat are successfully detected by the Canny algorithm.

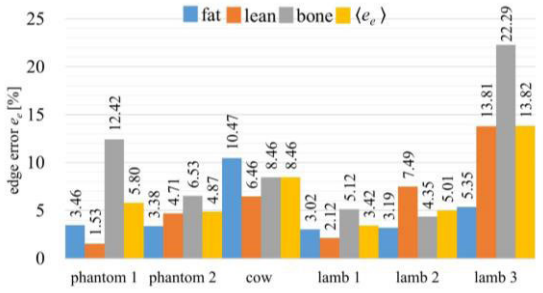

FIGURE 18. Edge error of meat composition e_e[%].

In order to evaluate the accuracy of detected meat composition edges ${}^k\Omega$, edge error e_e is defined as

$$ {}^k e_e = \left| \frac{{}^k\Omega - {}^k\Omega^{\text{true}}}{{}^k\Omega^{\text{true}}} \right| \times 100[\%] \tag{23} $$

where ${}^k\Omega$ is edge on k-th meat composition calculated from equation (14), ${}^k\Omega^{\text{true}}$ is k-th true meat composition. The bar chart in **Figure 18** shows e_e for agar phantoms, cow and lamb meats. The mean edge error $\langle e_e \rangle$ achieves to $\langle e_e \rangle = 5.80\%, 4.87\%, 8.46\%, 3.42\%, 5.01$ and 13.82% as shown in the yellow bar chart for agar phantom 1, agar phantom 2, cow, lamb 1, lamb 2 and lamb 3 respectively. The total mean edge error is achieved to $\langle \widetilde{e_e} \rangle = 6.90$ % which is relatively small. As a result, edge ${}^k\Omega$ as detected by Canny algorithm is close to the true edge ${}^k\Omega^{\text{true}}$.

V. CONCLUSION

High-speed and accurate meat composition imaging method has been proposed based on mechanically-flexible electrical impedance tomography (*mech-f*-EIT) with the k-nearest neighbour and fuzzy k-means machine learning approaches, which involves four steps. This method is qualitatively evaluated by using two agar phantoms, a cow meat and three lamb meat. This study concludes as follows:

REFERENCES

[1] L. Botti, C. Mora, and A. Regattieri, "Improving ergonomics in the meat industry: A case study of an Italian ham processing company," *IFAC-PapersOnLine*, vol. 48, no. 3, pp. 598–603, 2015.

[2] M. Marcoux, J. F. Bernier, and C. Pomar, "Estimation of Canadian and European lean yields and composition of pig carcasses by dual-energy X-ray absorptiometry," *Meat Sci.*, vol. 63, no. 3, pp. 359–365, Mar. 2003.

[3] A. D. Mitchell, A. M. Scholz, and V. G. Pursel, "Prediction of pork carcass composition based on cross-sectional region analysis of dual energy X-ray absorptiometry (DXA) scans," *Meat Sci.*, vol. 63, no. 2, pp. 265–271, Feb. 2003.

[4] P. V. Kremer, M. Förster, and A. M. Scholz, "Use of magnetic resonance imaging to predict the body composition of pigs *in vivo*," *Animal*, vol. 7, no. 6, pp. 879–884, 2013.

[5] X. Zhao, H. Zhuang, S.-C. Yoon, Y. Dong, W. Wang, and W. Zhao, "Electrical impedance spectroscopy for quality assessment of meat and fish: A review on basic principles, measurement methods, and recent advances," *J. Food Qual.*, vol. 2017, pp. 1–16, Jul. 2017.

[6] J. M. Khor, A. Tizzard, A. Demosthenous, and R. Bayford, "Development of a sensor network for dynamic boundary measurement in neonatal electrical impedance tomography (EIT)," in *Proc. IFMBE*, vol. 25, 2009, pp. 386–389.

[7] J. Hu and M. Soleimani, "Deformable boundary EIT for breast cancer imaging," *Biomed. Phys. Eng. Exp.*, vol. 3, no. 1, 2017, Art. no. 015004.

[8] A. M. Ravelli and P. J. Milla, "Detection of gastroesophageal reflux by electrical impedance tomography," *J. Pediatric Gastroenterol. Nutrition*, vol. 18, no. 2, pp. 205–213, Feb. 1994.

[9] J. Yao, G. Zhu, T. Zhao, and M. Takei, "Microfluidic device embedding electrodes for dielectrophoretic manipulation of cells—A review," *Electrophoresis*, vol. 40, no. 8, pp. 1166–1177, Apr. 2019.

[10] P. N. Darma, M. R. Baidillah, M. W. Sifuna, and M. Takei, "Real-time dynamic imaging method for flexible boundary sensor in wearable electrical impedance tomography," *IEEE Sensors J.*, vol. 20, no. 16, pp. 9469–9479, Aug. 2020.

[11] J. M. Khor, A. Tizzard, A. Demosthenous, and R. Bayford, "Wearable sensors for patient-specific boundary shape estimation to improve the forward model for electrical impedance tomography (EIT) of neonatal lung function," *Physiolog. Meas.*, vol. 35, no. 6, pp. 1149–1161, Jun. 2014.

[12] S. D. Gelidi, N. Seifnaraghi, A. Bardill, A. Tizzard, Y. Wu, E. Sorantin, S. Nordebo, A. Demosthenous, and R. Bayford, "Torso shape detection to improve lung monitoring," *Physiolog. Meas.*, vol. 39, no. 7, Jul. 2018, Art. no. 074001.

[13] J. Darde, H. Hakula, N. Hyvonen, and S. Staboulis, "Fine-tuning electrode information in electrical impedance tomography," *Inverse Problems Imag.*, vol. 6, no. 3, pp. 399–421, 2012.

[14] C. Gómez-Laberge and A. Adler, "Direct EIT Jacobian calculations for conductivity change and electrode movement," *Physiolog. Meas.*, vol. 29, no. 6, pp. S89–S99, Jun. 2008.

[15] A. Boyle, M. G. Crabb, M. Jehl, W. R. B. Lionheart, and A. Adler, "Methods for calculating the electrode position Jacobian for impedance imaging," *Physiolog. Meas.*, vol. 38, no. 3, pp. 555–574, Mar. 2017.

[16] A. Borsic, E. A. Attardo, and R. J. Halter, "Multi-GPU Jacobian accelerated computing for soft-field tomography," *Physiolog. Meas.*, vol. 33, no. 10, pp. 1703–1715, Oct. 2012.

[17] D. B. Geselowitz, "An application of electrocardiographic lead theory to impedance plethysmography," *IEEE Trans. Biomed. Eng.*, vols. BME–18, no. 1, pp. 38–41, Jan. 1971.

[18] J. Canny, "A computational approach to edge detection," *IEEE Trans. Pattern Anal. Mach. Intell.*, vol. PAMI-8, no. 6, pp. 679–698, Nov. 1986.

[19] P.-E. Danielsson and O. Seger, "Generalized and separable Sobel operators," in *Machine Vision for Three-Dimensional Scenes*. San Diego, CA, USA: Academic, 1990, pp. 347–379.

[20] C. Gabriel, S. Gabriel, and E. Corthout, "The dielectric properties of biological tissues: I. Literature survey," *Phys. Med. Biol.*, vol. 41, no. 11, pp. 2231–2249, Nov. 1996.

[21] M. W. Sifuna, M. R. Baidillah, A. Sapkota, and M. Takei, "A Cole-Cole dielectric relaxation analysis of albumin and γ-Globulins for protein quantification by electrical impedance spectroscopy," *Electroanalysis*, vol. 32, no. 5, pp. 1121–1129, May 2020.

[22] P. C. Hansen and D. P. O'Leary, "The use of the L-curve in the regularization of discrete ill-posed problems," *SIAM J. Sci. Comput.*, vol. 14, no. 6, pp. 1487–1503, 1993.

[23] F. Hecht, "New development in FreeFem++," *J. Numer. Math.*, vol. 20, nos. 3–4, pp. 251–265, 2012.

[24] S. C. Jun, J. Kuen, J. Lee, E. J. Woo, D. Holder, and J. K. Seo, "Frequency-difference EIT (fdEIT) using weighted difference and equivalent homogeneous admittivity: Validation by simulation and tank experiment," *Physiolog. Meas.*, vol. 30, no. 10, pp. 1087–1099, Oct. 2009.

[25] J. Dabek, K. Kalogianni, E. Rotgans, F. C. T. van der Helm, G. Kwakkel, E. E. H. van Wegen, A. Daffertshofer, and J. C. D. Munck, "Determination of head conductivity frequency response *in vivo* with optimized EIT-EEG," *NeuroImage*, vol. 127, pp. 484–495, Feb. 2016.

[26] M. Blackwell, C. Nikou, A. M. DiGioia, and T. Kanade, "An image overlay system for medical data visualization," *Med. Image Anal.*, vol. 4, no. 1, pp. 67–72, 2000, doi: 10.1016/S1361-8415(00)00007-4.

[27] P. J. Rousseeuw, "Silhouettes: A graphical aid to the interpretation and validation of cluster analysis," *J. Comput. Appl. Math.*, vol. 20, pp. 53–65, Nov. 1987.